

ARTICLE

Open Access

Bio-realistic synaptic characteristics in the cone-shaped ZnO memristive device

Andrey Sergeevich Sokolov¹, Yu-Rim Jeon¹, Sohyeon Kim¹, Boncheol Ku¹ and Changhwan Choi¹ 

Abstract

We demonstrate inherent biorealistic synaptic plasticity functions in the Pt/n-ZnO/SiO_{2-x}/Pt heterostructures, where the n-ZnO semiconductor is geometrically cone-shaped in the size of a few nanometers. The synaptic functions were achieved within a two-terminal, electroforming-free, and low-power rectifying diode-like resistive switching device. The important rate-dependent synaptic functions, such as the nonlinear transient conduction behavior, short- and long-term plasticity, paired-pulse facilitation, spike-rate-dependent plasticity and sliding threshold effect, were investigated in a single device. These characteristics closely mimic the memory and learning functions of those in biosynapses, where frequency-dependent identical spiking operations are mostly taking place, and we emulate these characteristics in the “Learning-Forgetting-Relearning” synaptic behavior. The switching dynamics in the cone-shaped n-ZnO semiconductor are correlated with the transport mechanism along the grain boundaries of the charged ion species, namely, oxygen vacancies and charged oxygen. The diffusion and generation/recombination of these defects have specific time scales of self-decay by virtue of the asymmetric profile of the n-ZnO cone defects. Finally, the essential biorealistic synaptic plasticity functions were discovered for the perspectives of dynamic/adaptive electronic synapse implementations in hardware-based neuromorphic computing.

Introduction

With a power consumption of ~20 watts and a volume of approximately 1200 cm³, our brain is an amazing computing instrument for tackling complex computational tasks, such as visual image recognition, precise voice detection, and control of motor functions. Consisting of approximately 10¹¹ neurons and 10¹⁵ synapses, our brain computes in a massive parallel mode by sending spiking signals from preneuron to postneuron. Typically, neurons are connected via the dendritic tree and axons, and the place of each connection is called a synapse, where spiking signals change the synaptic weight (w_{ij}) and the actual computation and memory storage takes place^{1,2}. To save power and perform sufficient neuromorphic computing, numerous synapses are required, and this is where emerging memory technologies come into play. Specifically, the memristors, which are two-terminal

electrical devices of those internal resistance states governed by combined ionic diffusion dynamic and charge trap/detrapping processes, have garnered interest in the use of synapse devices, particularly, the realization of important “learning-experience behavior” functioning^{2–5}. The key advantages of memristors being applied as synapses are due to their fast switching speed, low-power consumption, cross-bar integration, and unique binary and analog resistance switching properties, which make them suitable candidates for a variety of applications, including reconfigurable circuits, novel memories, and future hardware-based neuromorphic systems^{6–10}.

To date, many research works are focused on reproducing basic synaptic learning rules, namely, spike-timing-dependent plasticity (STDP), by utilizing various types of memristors, typically, oxygen-deficient and metal cation-based filament operation resistive switching devices^{11–13}. However, many of the restrictions of these memristors, such as their electroforming process, stochastic multifilament formation, and, importantly,

Correspondence: Changhwan Choi (cchoi@hanyang.ac.kr)

¹Division of Materials Science and Engineering, Hanyang University, Seoul 04763, Republic of Korea

© The Author(s) 2019



Open Access This article is licensed under a Creative Commons Attribution 4.0 International License, which permits use, sharing, adaptation, distribution and reproduction in any medium or format, as long as you give appropriate credit to the original author(s) and the source, provide a link to the Creative Commons license, and indicate if changes were made. The images or other third party material in this article are included in the article's Creative Commons license, unless indicated otherwise in a credit line to the material. If material is not included in the article's Creative Commons license and your intended use is not permitted by statutory regulation or exceeds the permitted use, you will need to obtain permission directly from the copyright holder. To view a copy of this license, visit <http://creativecommons.org/licenses/by/4.0/>.

repeatability of analog fashion resistance states change, have yet to be overcome to effectively apply these memristors in large-scale memory cross-bars, which serve as one of the main building blocks for hardware-based neuromorphic systems^{4,14,15}. Due to these limitations, the system implementation of even basic learning rules, such as STDP, is becoming a difficult task. The overlapping spiking signals arriving from pre- and postsynaptic neurons have to be programmed manually (in terms of pulse duration and amplitude) to obtain the desired synaptic behavior, which could bring high complexity and restrictions to the neuromorphic circuit^{13,16}. Recently, to overcome these problems, a memristor with diffusive dynamics¹⁷ and a second-order memristor¹⁸ have been proposed, where a decaying STP-term allows STDP to be implemented with non-overlapping spiking. It is analogous to biological synapses, in which the overall internal dynamic (information encoding) is governed via spatio-temporal encoding, i.e., by sending identical non-overlapping spikes, where the sign of the synaptic trans-conductance strongly depends on the history of applied spikes¹⁹. However, the trans-conductance is gradually increasing when the high-frequency stimulation (HFS) arrives or is gradually decreasing when the low-frequency stimulation (LFS) arrives to the biosynaptic connection^{20–22}.

To tackle the above issues, the usage of interface-based resistive switching (RS) devices may be a feasible approach due to their highly repeatable analog redistribution of resistance states, whereas electroforming-free behavior eliminates randomness in the resistance states, which is typically generated in memristors with filament formation and growth^{23–25}. Metal-oxide Schottky-like contact junctions are part of the family of interface-based RS and represent rectifying diode-like switching characteristics within the important framework of electroforming-free operation, large resistance R_{ON}/R_{OFF} ratio and continuously tunable resistance states, making them the most suitable option for mimicking real biosynaptic behaviors, while keeping scaling requirements down^{26–28}. The shortage of retention time in these devices, as proved by Hansen et al.²⁹, can be solved with inserting a specific tunneling barrier at the back of the Schottky-like contact of the device. Nevertheless, with the benefits of the identical spiking scheme and the retention times ranging from a few seconds to a few thousands of seconds, the possibilities of implementations of w_{ij} dynamically working in these memory retention time scales provide the remarkable conditions to obtain the easy training/learning schemes of a spiking neural network¹⁴.

In this study, we investigate the reverse biased $I-V$ characteristics of rectifying diode-like Pt/n-ZnO/SiO_{2-x}/Pt synaptic heterostructures, where semiconducting n-ZnO thin films were intentionally cone-shaped in SiO_{2-x} matrix protrusions to reduce excessive current leakage

and to form one-side variable diode-like conditions. Within the oxygen vacancies and charged oxygen accumulation/self-recombination processes in the cone-shaped n-ZnO memristor-based framework, the device's short-term state (plasticity) is assumed to be controlled by excessive ion charge traps at the Pt/n-ZnO Schottky contact, whereas the device long-term state (plasticity) is assumed to be guided by the relaxation time of accumulated oxygen vacancies near the top Pt/n-ZnO interface, coming from the inside-cone oxygen-deficient nanocrystalline n-ZnO_{1-x} thin film. In addition, natural decay induced by accumulated oxygen vacancies and charged oxygen provides an internal timing, ranging in the intervals of a few milliseconds (1–5 ms) to a hundred milliseconds (50–100 ms), and a gradual conductance change mechanism similar to the synaptic influx/extrusion of Ca²⁺ ions concentrated in the biosynapses^{30,31}. These effects empower the device to exhibit essential rate- and time-dependent behaviors dually, i.e., short-term as pair-pulse facilitation (PPF)³² and long-term as a strong accumulation of charged species, i.e., oxygen vacancies, with their long retention time scales by using identical non-overlapping voltage spikes with varied frequencies. Specifically, the biological synapse strength (conductance) is varied by the influx/extrusion processes of the Ca²⁺ ions, in an analogous fashion as the oxygen vacancies in-/out-drift as the semiconducting device operates, in terms of the following: 1) diffusion—oxygen vacancies drift under the electric field (E), 2) concentration balance—the stronger the electric field applied, the more oxygen vacancies induced, 3) regulating role—elevated concentration of oxygen vacancies provides enhanced trans-conductance of the device. Finally, with the functionalities of Ca²⁺ ions, such as the diffusion mechanism, balance of concentration and regulating roles in their respective biosystems³³, we experimentally demonstrate both short- and long-term potentiation (STP and LTP), including the important synaptic functions that we explored extensively in our single device, such as PPF, spike-rate-dependent plasticity (SRDP), sliding threshold (θ_m) effect, and the important “Learning-Forgetting-Relearning” synaptic behavior.

Methods

Materials

Commercially available p-Si/SiO₂ substrates, where p-Si specified with (100) orientation, p-type boron dopant, a resistivity of 1–10 Ohm-cm, a thickness of 500–550 μm , and silicon oxide (SiO₂) wet oxidation \sim 300 nm physical thickness, were used. The DEZ (diethyl zinc-C₂H₅-Zn-C₂H₅) precursor from UP Chemical Co. Ltd. (Pyeongtaek, Republic of Korea) was used in the standard atomic layer deposition (ALD) reactor machine (Model: Atomic-Class) CN1 Co. Ltd. (Hwaseong, Republic of Korea).

Device fabrication

The fabrication of two-terminal Pt/n-ZnO/SiO_{2-x}/Pt synaptic heterostructures consists of platinum (Pt) electrodes serving as the top and bottom electrical contacts. The surface of the p-Si/SiO₂ substrates was thoroughly cleaned by acetone, ethanol, isopropyl alcohol (IPA), and deionized water in sequence and dried by high-quality nitrogen gas (99.99% N₂). The titanium (Ti), serving as an adhesion layer, and platinum (Pt) thin films with the thicknesses of ~70 and ~80 nm, respectively, were deposited by an El-5 ULVAC model e-beam evaporator without breaking vacuum. Thereafter, p-Si/SiO₂/Ti/Pt substrates were transferred to a Unaxis VL-LA-PECVD chamber and fully stoichiometric SiO₂ with a thickness of ~100 nm was grown with a deposition rate of 40 nm/min and a process temperature of 200 °C. Subsequently, p-Si/SiO₂/Ti/Pt/SiO₂ substrates were cut into square pieces of 2 × 2 cm² and processed for via-hole (~4 μm) development by means of a photolithography (deep ultra violet) mask and etching in a buffer oxide etchant (BOE) consisting of the standard 6:1 volume ratio of 40%-NH₄F in H₂O to 49%-HF in H₂O, respectively. The BOE etching conditions were varied next (15 s, 1 min 30 s) to gradually reduce the thickness of the SiO₂ in the via-hole pattern and to form cone-shape protrusions in the SiO₂ dielectric matrix to deposit the n-ZnO thin films later. The n-type semiconductor ZnO thin films were deposited in the ALD reactor chamber at 170 °C with a precursor and a water oxidant time of 0.4 s. After the second lithography process at the via-hole area, the Pt top electrode with a thickness of ~97 nm was grown in 100 × 100 μm² square patterns by using direct sputtering with Ar plasma at room temperature. The complete device scheme is represented in Fig. 1a.

Characterization and device test

The structural properties of fabricated Pt/n-ZnO/SiO_{2-x}/Pt synaptic heterostructures were characterized using scanning transmission electron microscope (STEM) analysis. The cross-sectional TEM samples were prepared by a common focus ion beam method, utilizing an FEI Quanta 3D FEG dual-beam instrument. The upper device surface was protected by a resin layer, then the device was cut out in the exact via-hole region and sliced to thickness of a few hundred nanometers. The high angle annular dark field (HAADF)-STEM images were obtained using JEOL JEM-2100F TEM operated at 200 kV and a lattice resolution of ~0.1 nm. The FIB and TEM experiments were performed in the Korea Advanced Nano Fab Center (KANC). Electrical characterization of the Pt/n-ZnO/SiO_{2-x}/Pt synaptic heterostructures were investigated in ambient air under controlled temperature (~25 °C) and humidity (~28%) with a Keithley 4200—SCS semiconductor parameter analyzer by applying sweeping

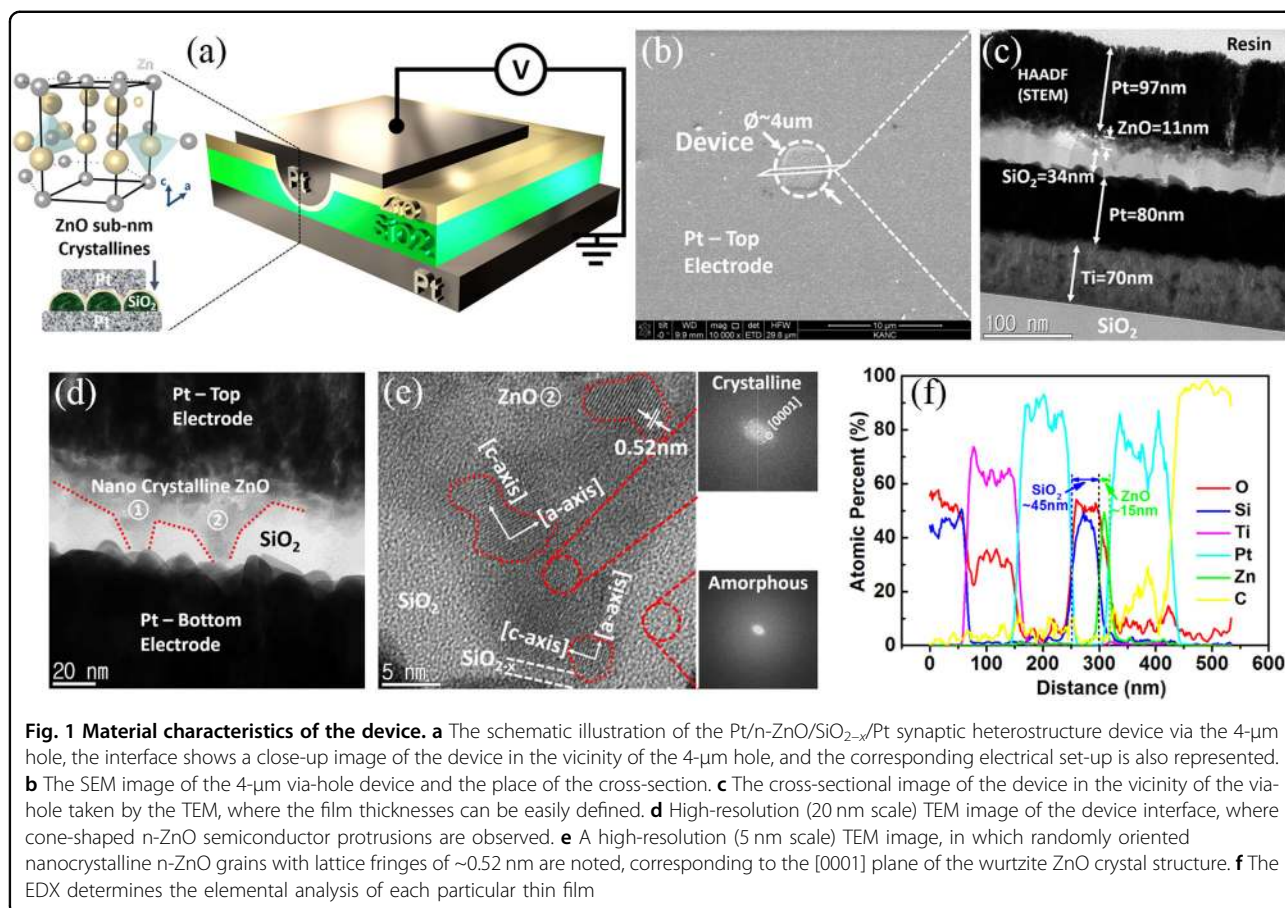
voltages and specified voltage pulses with a 4225—PMU ultrafast *I*–*V* module and two 4225—RPM remote amplifier/switch modules. The humidity test was performed with a homemade set-up chamber, where N₂ gas drying and a humidifier were utilized to control the level of humidity in the range of 0% RH to 100% RH by ~5 ± 1% RH per step.

Results and discussion

Material characteristics and switching mechanism

The Pt/n-ZnO/SiO_{2-x}/Pt synaptic heterostructures illustrated in Fig. 1a consist of two platinum (Pt) inert electrodes, sandwiching a double switching layer of semiconducting nanocrystalline (NC) n-ZnO and thin SiO_{2-x} dielectric thin films. The cross-sectional view shows the effective contact area within the device and the corresponding electrical characterization set-up. The enlarged interface area reflects the cone-shaped NC n-ZnO deposited via intentionally made protrusions in the SiO₂ dielectric thin film (see Methods section). Scanning electron microscopy (SEM) of the planar view confirms the 4 μm via-hole device size in Fig. 1b. Further, we have obtained cross-sectional images of the via-hole device by utilizing HAADF-STEM microscopy, as shown in Fig. 1c–e. A smooth Pt/SiO₂ interface is observed and a quite rough Pt/n-ZnO interface is found, due to the BOE pretreatment of the SiO₂ dielectric thin film. However, as we will show later, this rough interface has no impact on the device reliability performance. The thicknesses of the top and bottom electrodes, which are ~97 and ~80 nm, respectively, as well as for the n-ZnO semiconductor (~11 nm) and SiO₂ dielectric (~34 nm) can be easily defined. The darker contrast of STEM reflects a heavier element with a corresponding higher atomic number.

Therefore, here, the n-ZnO and SiO₂ thin films can be distinguished clearly and, importantly, the existence of a number of cone-shaped n-ZnO protrusions in the intentionally protrusion-formed SiO₂ dielectric thin films can be clearly observed. To further investigate the cone-shaped n-ZnO via SiO₂ dielectric protrusions, high-resolution STEM images were taken, as shown in Fig. 1d, e. As confirmed from the STEM images, the multiprotrusions of sizes of ~10–15 nm were formed in the SiO₂ dielectric under applied BOE wet etching treatment in the vicinity of the 4 μm via-hole device, which is found completely filled with NC n-ZnO thin films. Particularly, the cone-shaped NC n-ZnO thin film consists of a few nanometers of randomly oriented and shaped polycrystalline grains. From the high-resolution STEM image shown in Fig. 1e, we were able to determine the growth direction and crystallographic orientations of the polycrystalline grains. The data shows that the lattice fringes of the randomly oriented polycrystalline grains in most cases measured to be ~0.52 nm, corresponding to



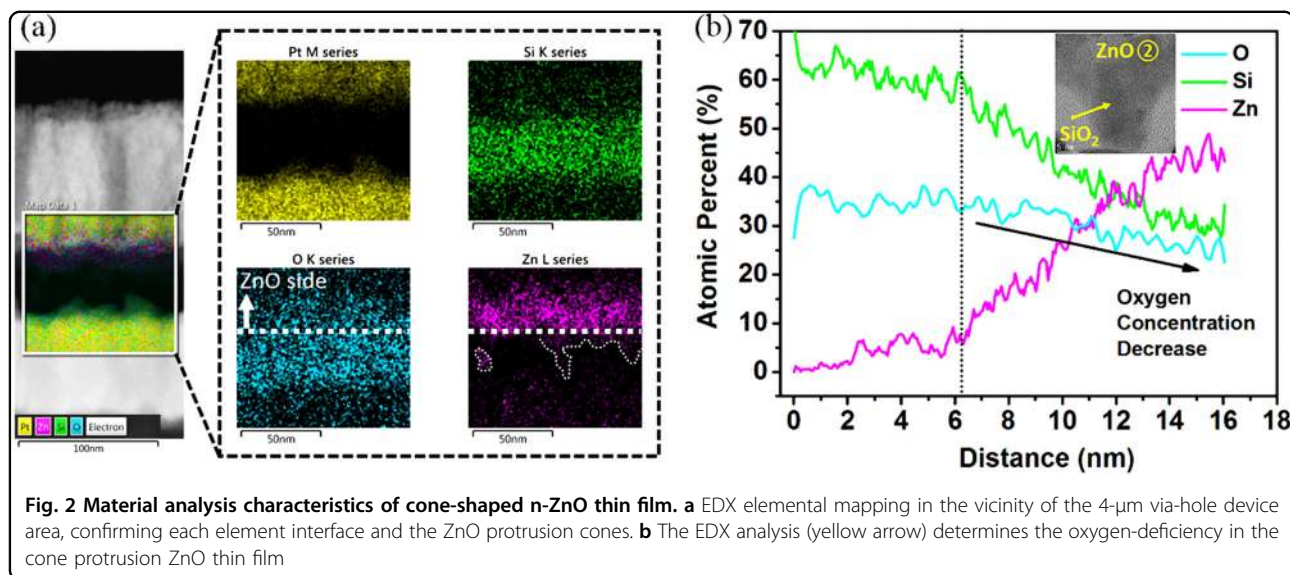
the [0001] plane of the wurtzite ZnO crystal structure with the growth direction along *c*-axis^{34,35}. In addition, the diffraction patterns with Fast Fourier transformation (FFT) confirm the crystalline nature of the n-ZnO thin films, whereas the SiO₂ dielectric films are found in the fully amorphous phase. In Fig. 1f, the energy-dispersive X-ray spectroscopy (EDX) analysis determines the elemental atomic ratio of each particular element at a given interface and according to the thicknesses of the thin films.

Further evidence of the stoichiometric SiO₂ thin film and nanocrystalline protrusions of n-ZnO thin film can be seen from the EDX mapping analysis in Fig. 2a.

To investigate the existence of oxygen-deficient regions in the n-ZnO thin film, the EDX analysis was further utilized. The near stoichiometric compositional profile of n-ZnO thin film close to the top Pt electrode was found, implying the presence of \sim 40 atom % Zn and \sim 40 atom % O at the top of the Pt/n-ZnO interface, as shown in Fig. S1 (see supporting information). However, the cone protrusion area of n-ZnO thin film distinctly contains the high oxygen-deficient region, detecting the presence of \sim 45 atom % Zn and \sim 24 atom % O by the EDX selected elemental profile (yellow arrow), as shown in Fig. 2b. The high oxygen-deficiency of the n-ZnO cone protrusion is

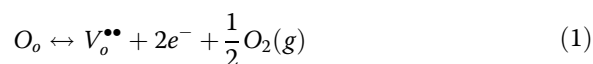
probably introduced by the formation of natural defects, such as oxygen vacancies (V_o 's), nonlattice oxygen (O_o^x), and zinc interstitials (Zn_i), in the randomly oriented crystalline grains during n-ZnO thin film deposition³⁶. As the result, we expect that the asymmetric profile would be formed out of oxygen and oxygen-deficiency regions between the top Pt/n-ZnO interface and the n-ZnO cone protrusion.

We discuss the switching mechanism of rectifying diode-like Pt/n-ZnO/SiO_{2-x}/Pt synaptic heterostructures and show that under reverse voltage bias conditions, this device can exhibit important time-rated plasticity characteristics, such as STP, LTP, PPF, θ_m effect, etc., similar to a biological synapse. Figure 3 shows the proposed switching mechanism of the device with the cone-shaped n-ZnO semiconductor. The HRTEM image of NC n-ZnO incorporated into the SiO₂ dielectric matrix is shown in Fig. 3a. The equivalent circuit element of this device can be represented as one diode (1D), i.e., a metal-semiconductor Schottky junction (top Pt/n-ZnO interface), and one resistor (1R), i.e., the bulk of NC n-ZnO thin film and a very thin SiO_{2-x} tunnel barrier. It is worth mentioning that this combinational 1D1R element has already been specified as an electronic synapse



in the circuits for neuromorphic computational systems^{37,38}. Here, we observe the cone-shaped n-ZnO semiconductor with randomly oriented nanocrystallines, which with contact to each other will form many GBs connections. The primary transient conduction is believed to take place at these GBs connections, according to the defect chemistry considerations and high resistivity of monolithic single-crystal ZnO material^{35,39,40}. It is also known that the ZnO possesses covalent bonding (Zn–O bonding), which allows the high mobility of oxygen (O_o) atoms; however, in ZnO, the most likely oxygen vacancies formation (~ 1 eV) are V_o^\bullet and $V_o^{\bullet\bullet}$ (single/double positive charged)^{41,42}. Based on the careful speculations in the EDX analysis above, our device consists of two regions, as follows: first, a nearly stoichiometric ZnO thin film at the Pt/n-ZnO top interface, and second, highly oxygen-deficient (zinc-Zn metal rich) region via cone-shape, confirming ZnO_{1-x} oxygen-deficient thin film existence as shown in Fig. 3a (on the right side). Chen et al.⁴³ reported previously that the resistive switching in ZnO material is caused by the migration of oxygen ions, leading to the transformation between Zn-dominated ZnO_{1-x} and ZnO thin films. At the same time, Huang et al.⁴⁴ researched the homogeneous resistive switching in the ZnO thin films, discovering the current compliance-controlled homogeneous interface resistive switching, which is attributed to an asymmetric balance of the Schottky barrier height. Considering the above, the next resistive switching mechanism of our rectifying diode-like Pt/n-ZnO/SiO_{2-x}/Pt synaptic heterostructures is proposed as shown in Fig. 3b. In the initial resistance state, (i) the device consists of an asymmetric concentration profile out of oxygen and oxygen-deficiency in the two sides of

the device, i.e., a metal-semiconductor Pt/n-ZnO Schottky interface and the cone-shape filled with ZnO_{1-x} oxygen-deficient thin film, according to the EDX elemental analysis. Further, under the reversed voltage bias, (ii) the high oxygen vacancies generation/accumulation driven by the inside-cone concentrated electric field (E) and elevated temperature (Joule heating) can push the oxygen vacancies towards the top Pt/n-ZnO blocking Schottky interface. Allen et al.⁴⁵ studied the influence of oxygen vacancies on the Schottky contacts of semiconductor ZnO thin films and found that the oxygen vacancies tend to pin the ZnO Fermi level close to the V_o ($+2;0$) defect level below the conduction band minimum. Considering this, we speculate that the increased concentration of oxygen vacancies near the top Pt/n-ZnO interface will gradually reduce the Schottky barrier height and will induce promoted transient conduction behavior of the device. The subsequent increased concentration of oxygen vacancies, i.e., V_o^\bullet and $V_o^{\bullet\bullet}$, according to the Kroger-Vink notation can be described as following Eq. (1), as follows:



where the bottom register is the position and the upper register is the charge, respectively. We note that our device system is closed (the via-hole device structure with top and bottom Pt electrodes and SiO₂ surrounding); therefore, from Eq. (1), the release of gaseous oxygen ($1/2\text{O}_2$) will be preserved and pushed laterally by the extended creation of oxygen vacancies and E , and also, the released oxygen will not oxidize the top Pt electrode (platinum is inert metal). Furthermore, under removed negative voltage bias, (iii) the recombination

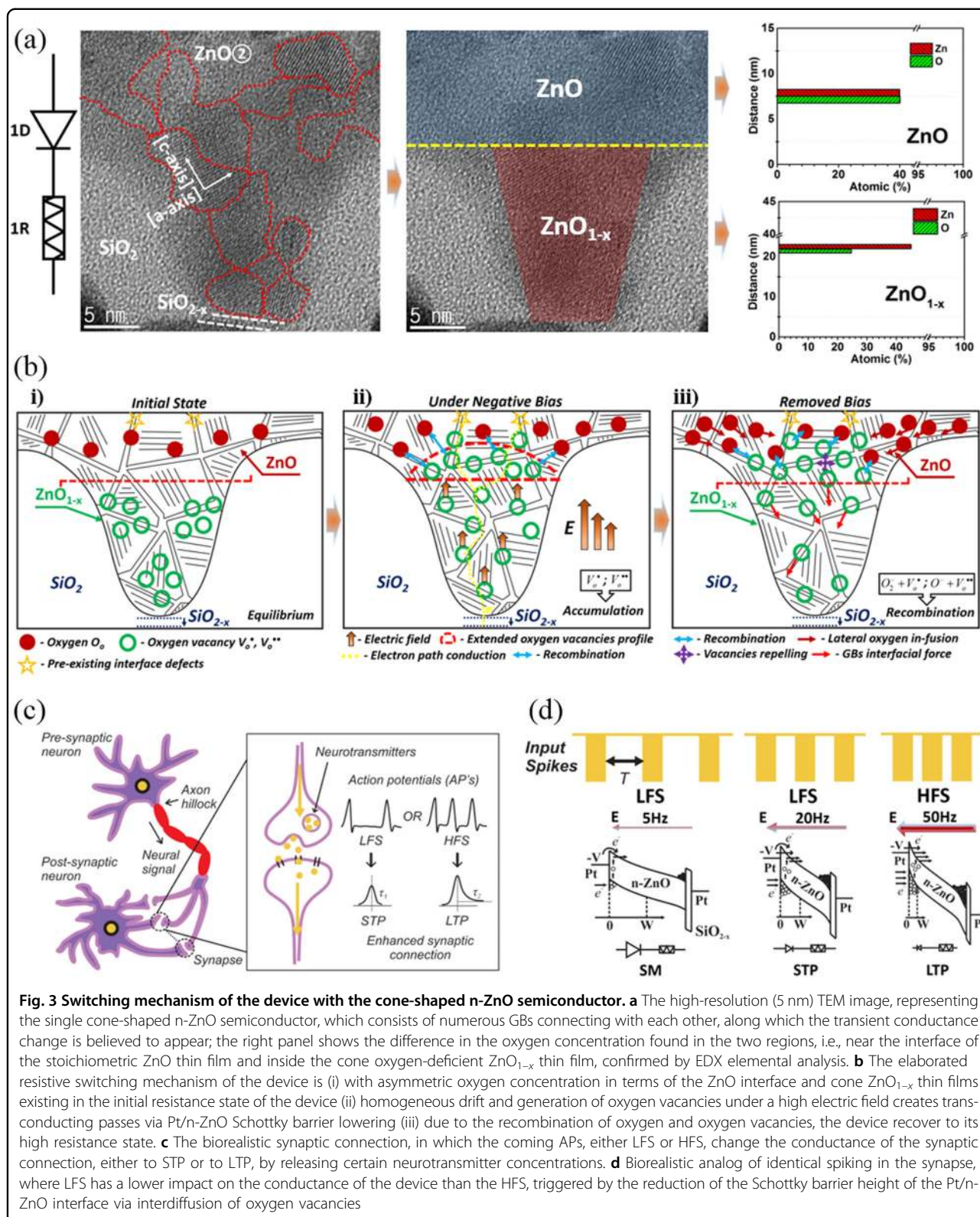


Fig. 3 Switching mechanism of the device with the cone-shaped n-ZnO semiconductor. **a** The high-resolution (5 nm) TEM image, representing the single cone-shaped n-ZnO semiconductor, which consists of numerous GBs connecting with each other, along which the transient conductance change is believed to appear; the right panel shows the difference in the oxygen concentration found in the two regions, i.e., near the interface of the stoichiometric ZnO thin film and inside the cone oxygen-deficient ZnO_{1-x} thin film, confirmed by EDX elemental analysis. **b** The elaborated resistive switching mechanism of the device is (i) with asymmetric oxygen concentration in terms of the ZnO interface and cone ZnO_{1-x} thin films existing in the initial resistance state of the device (ii) homogeneous drift and generation of oxygen vacancies under a high electric field creates transconducting passes via Pt/n-ZnO Schottky barrier lowering (iii) due to the recombination of oxygen and oxygen vacancies, the device recover to its high resistance state. **c** The biorealistic synaptic connection, in which the coming APs, either LFS or HFS, change the conductance of the synaptic connection, either to STP or to LTP, by releasing certain neurotransmitter concentrations. **d** Biorealistic analog of identical spiking in the synapse, where LFS has a lower impact on the conductance of the device than the HFS, triggered by the reduction of the Schottky barrier height of the Pt/n-ZnO interface via interdiffusion of oxygen vacancies

processes of the extended oxygen vacancies profile and previously laterally pushed oxygen will occur. Subsequently, the recovery of the stoichiometric ZnO thin film

near the top of the Pt/n-ZnO interface will appear, leading to the back-increased Schottky barrier height and, therefore, the initial resistance state of the device.

The proposed reduction reactions of the oxygen vacancies, i.e., V_o^\bullet and $V_o^{\bullet\bullet}$, can be followed by:



It is also worth mentioning that additional factors, such as oxygen vacancies repelling, GBs stress/strain release and crystalline ZnO_{1-x} phase transformation, could also participate in the resistive switching behavior; however, in comparison to the oxygen vacancies formation and diffusion, their influence seems to be minor in the device.

Additionally, the resistive switching mechanism of the device under the positive bias is shown in Fig. S2. Further, the relationships between a real biological synapse and rectifying diode-like Pt/n-ZnO/SiO_{2-x}/Pt synaptic heterostructures are briefly discussed. Figure 3c shows the schematic of a biological synapse. The synaptic cleft is an area between the axon of a presynaptic neuron and the dendrite tree of a postsynaptic neuron⁴⁶. When spikes, or action potentials (APs), arrive to the presynaptic neuron connection, the edge of synaptic bulb starts to release neurotransmitters to the cleft, which bind with the receptors of the postsynaptic neuron to construct conductive ion channels for signal transmission. Accordingly, the enhancement of a postsynaptic potential (PSP) occurs, whose amplitude can be defined by the connection strength, namely, the synaptic weight, which can last in the range of a milliseconds, implying the short-term potentiation, to a few seconds/minutes, implying the long-term potentiation, in respect to the rate of stimulation^{32,33,47}. Importantly, in neurobiological studies, LFS and HFS by APs could cause short/long-term conductivity enhancement in the synaptic cleft, respectively^{20–22}. This is called synaptic plasticity activation, which is argued as being a basis of sensory memory (SM), STP, and LTP in the psychological model of human brain memorization⁴⁸. Fig. 3d shows the schematic of the bandgap construction of Pt/n-ZnO/SiO_{2-x}/Pt synaptic heterostructures, operating under identical input spikes with varied frequencies, i.e., LFS and HFS. As has been previously reported, the diffusion of oxygen vacancies in the memristors is strongly correlated with the impact effects induced by high E and Joule heating, whereas identical different frequency spikes are applied¹⁸. Therefore, we speculate that under the impact of concentrated E , the accumulation and homogeneous diffusion of oxygen vacancies, i.e., V_o^\bullet and $V_o^{\bullet\bullet}$, in the cone-shaped n-ZnO thin films occur. With the benefits the cone geometry created, i.e., the non-equilibrium concentration profile of oxygen and oxygen vacancies, the ions back-diffusion time constants could be well correlated, while modifying the n-ZnO semiconductor oxygen-deficiency profile and the barrier height of the metal-semiconductor Schottky contact^{40,45,49,50}. With negative spiking applied, when the LFS

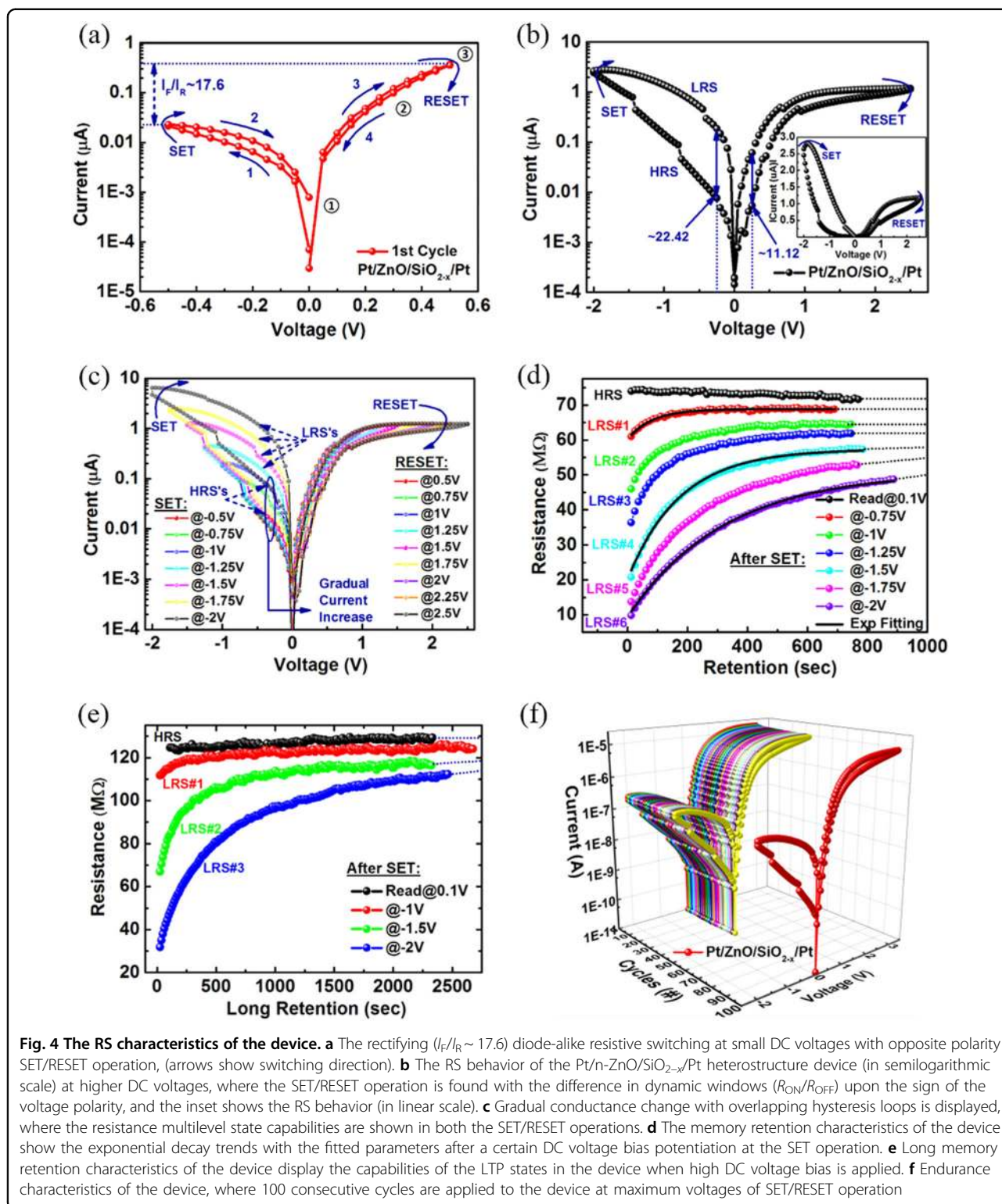
arrives to the device, one spike starts to trigger a small accumulation and a drift of charged species, however, due to the long-time interval to the next spike, the triggered concentration of accumulated defects will back-diffuse to its equilibrium state and no enhancement of transient conduction is observed. This state can be ascribed as the SM state, where the initial state of current transient conduction behavior occurs. Later, as the LFS time intervals between spikes become shorter, the drift of ions, i.e., V_o^\bullet and $V_o^{\bullet\bullet}$ oxygen vacancies, have less time to diffuse back and in sequence the slow accumulation of charged ions occurs, promoting the gradual increase of transient conduction behavior. This state without external spiking can last only for a few seconds, since the back-diffusion of ions exists, and they can be regarded as STP states. On the other hand, when the HFS arrives to the device, due to the short time intervals between spikes and the accordingly strong impact of the high electric field (E) and the Joule heating effects on the drift diffusion of oxygen vacancies, a strong and fast accumulation of the defects is observed, causing the intensive gradual increase of transient conduction behavior. Without external spiking, this state can last for hundred/thousands of seconds, indicating LTP states, similar to the plasticity effects observed in biological synapses, as we discuss later.

The resistive switching characteristics of the device

Figure 4 displays the I - V characteristics of the Pt/n-ZnO/SiO_{2-x}/Pt synaptic heterostructures, namely, RS behavior, memory retention loss, and cycling endurance. First, the rectifying RS behavior of each device was observed without any electroforming step, indicating relatively high intrinsic conductivity of NC n-ZnO semiconductor thin films, and the current level is found in the nano-ampere (nA) range, as shown in Fig. 4a. We estimate the rectifying RS behavior of the device by the DC voltage sweeping mode as $0\text{ V} \rightarrow 0.5\text{ V} \rightarrow 0\text{ V} \rightarrow -0.5\text{ V}$ and disclose the diode-like rectifying ($I_F/I_R \sim 17.6$) resistive switching behavior with opposite switching polarity of SET/RESET memory operation. The rectifying diode current behavior can be described with the thermionic emission theory⁵¹, and it is dominated by (1) the recombination/generation current, (2) the diffusion current, and (3) the diffusion current at high level injection, for forward bias, and defined as Eq. 4, as follows:

$$I_S = I_R \left(e^{\frac{eV}{nk_B T}} - 1 \right) \quad (4)$$

where T and k_B are the temperature and Boltzmann constant, respectively, and n is an ideality factor, which indicates the deviation from the ideal diode characteristics. However, when a higher DC voltage sweeping bias is applied as $0\text{ V} \rightarrow 2.5\text{ V} \rightarrow 0\text{ V} \rightarrow -2\text{ V} \rightarrow 0\text{ V}$, the extinction of rectifying diode-like characteristics and



nearly Ohmic transient conduction behavior is observed in the device at the negative voltage side, as represented in Fig. 4b (in semilogarithmic scale) and its inset (in linear scale). Interestingly, the low resistance state (LRS) and

high resistance state (HRS) ratio differences of $R_{ON}/R_{OFF} \sim 11.12$ at positive bias and $R_{ON}/R_{OFF} \sim 22.42$ at negative bias were found, respectively. We believe that this is attributed to the oxygen-deficient asymmetric

concentration profile found in the n-ZnO thin film via the cone geometry, which is affected by the sign of the DC voltage bias, and according to the balance in concentrations of charged ion species, namely, oxygen vacancies V_{O} s and oxygen O_2^- , changing by their internal diffusion ions dynamic as discussed in the switching mechanism section. To exhibit biorealistic synaptic characteristics, the device should possess analog-type multilevel cell resistive switching ability, which we explore in Fig. 4c.

When negative DC voltage bias is applied gradually as ($-0.5 \text{ V} \rightarrow -0.75 \text{ V} \rightarrow \dots$), the current increases in monotonic fashion with overlapping hysteresis loops while switching the device step-by-step from HRS to LRS. This procedure corresponds to the SET operation mode of the memory. Similar steps with DC positive bias applied ($0.5 \text{ V} \rightarrow 0.75 \text{ V} \rightarrow \dots$) and the current decrease in monotonic fashion corresponds to the RESET operation mode of the memory device and is represented in Fig. S3. Here, we note the fact that the current change difference between the HRS and LRS at the SET operation is approximately 20 times higher than at the RESET operation, which is probably due to effective accumulation of charged ion species under the negative bias near the interface and corresponding top Pt/n-ZnO Schottky barrier lowering, whereas their fast recombination occurs under the positive bias. Additionally, since the accumulated oxygen vacancies have specific time scales to decay, we explore the synaptic characteristics via the transient conduction behavior of the device only at the SET operation mode of the device hereafter. In Fig. 4d–e the retention memory characteristics of the Pt/n-ZnO/SiO_{2-x}/Pt synaptic heterostructures are discussed. Prior to any DC voltage bias applied, the device was measured at a small reading voltage of 0.1 V to obtain the memory's initial resistance state, i.e., HRS. Later, the -0.75 V voltage bias was applied once and the device was immediately set under the same reading voltage of 0.1 V and LRS#1 was measured. After a considerably long-time, the device was confirmed to return to its initial resistance state, i.e., HRS. Interestingly, the device returns to its HRS even if the device was subjected to the higher DC negative voltage biases, namely, -1 V , -1.25 V , etc., indicating a device plasticity capability similar to that of a biological synapse²². Furthermore, we observe that all measured low resistance states from LRS#1 to LRS#6 can be well-fitted (black curves in Fig. 4c) with the stretched-exponential function (SEF), which has notable similarities with a human memory forgetting/retention curve in psychological studies⁵², and can be written as follows:

$$I(t) = I_0 + A \exp\left(\frac{-t}{\tau}\right) \quad (5)$$

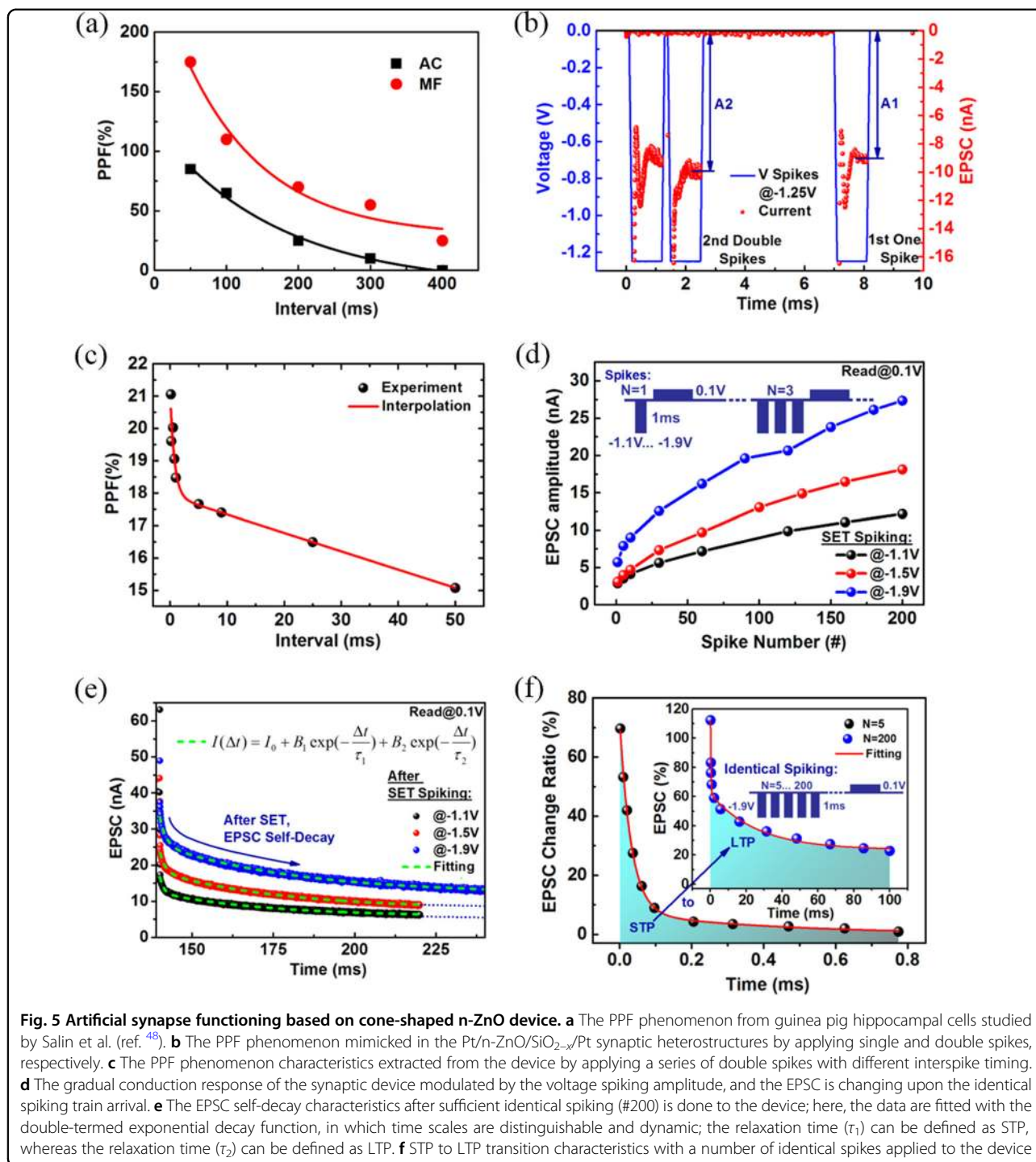
where $I(t)$ is the relaxation function, I_0 is the constant background, A is the prefactor, and τ is the characteristic

relaxation time. By examining Eq. (5), we expect a rapid drop when $t \ll \tau$, followed by a quite slower decay when $t \gg \tau$. Indeed, this tendency is coincident with the description of human memory loss, where a fast initial decline is followed by a slow, long decay⁵³. Therefore, in our device, as shown in Fig. 4d, the τ can be used to define the STP states, when $t \ll \tau$ and lasts only from a few to decades of seconds, whereas LTP states can be defined, when $t \gg \tau$ and it can last from a few hundreds to thousands of seconds. This is also similar to the synaptic plasticity behavior, where after learning, the rapid changes in cytoskeletal and adhesion molecules contribute to the STP, whereas later changes, which depend on the protein synthesis and early modifications, could result in the persistence of LTP^{33,47,54}. In addition, we extract the parameters of the fitted SEF function (Eq. 5) for some low resistance states, i.e., LRS#1, LRS#4, and LRS#6, to show how they evolve in time, as shown in Table 1.

Further, as displayed in Fig. 4e, we investigate the long memory retention characteristics of the device to elucidate the resolution of the time scales of the device to exhibit synaptic LTP states. It is found that with higher DC negative voltage applied, the device can exhibit more long-termed transient conduction characteristics. This LTP state is important for the dynamic hardware-based neuromorphic systems, where the long-time storage of w_{ij} , high device resistivity, and large resistance dynamic window, i.e., $R_{\text{ON}}/R_{\text{OFF}}$ ratio, are critical to perform the learning operation efficiently. Furthermore, we studied the endurance characteristics of the device by applying DC sweeping voltages, as $0 \text{ V} \rightarrow 3 \text{ V} \rightarrow 0 \text{ V} \rightarrow -2 \text{ V} \rightarrow 0 \text{ V}$, in sequence and repeat them in 100 cycles continuously, as shown in Fig. 4f. No notable degradation of the device was observed, indicating highly uniform and reliable resistive switching characteristics, which is required for the proper electronic synapse operation. Moreover, the Device-to-Device resistive switching variation has been measured, as shown in Fig. S4. The pulse endurance characteristics of the device showed the cycling durability of the device up to 50,000 cycles without notable degradation, as displayed in Fig. S5. The temperature-dependent device resistive switching characteristics have also been evaluated, as depicted in Fig. S6. The reduction of hysteresis loops with an increase of the temperature is found, which is attributed to the rearrangement of oxygen

Table 1 Summarized parameters of SEF, Eq. (5)

$R_{\text{states}}/\text{parameters}$	I_0	A	$\tau, \text{ s}$
LRS#1	6.88	-8.63	83.33
LRS#4	5.73	-3.72	175.44
LRS#6	5.092	-4.15	322.58



in the ZnO thin films and subsequent improvement of the defective sites of the Pt/n-ZnO Schottky interface and the cone oxygen-deficient ZnO_{1-x} region, leading to the improvement of the diode rectifying behavior. However, when the temperature decreases back to 30 °C, full recover of the hysteresis loops are observed. Under the “freeze” conditions (~0 °C), the device revealed the overall

current reduction of hysteresis loops, however, the SET/RESET operations were sustainable, as shown in Fig. S7. This is attributed to the decreased mobility of interface defects at the Pt/n-ZnO interface and the decreased mobility of the oxygen vacancies in the cone ZnO_{1-x} thin film region, leading to overall current leakage reduction of the device. During the humidity test, no variation of the

resistance state of the device was found, indicating the ability of the device to work sustainability in wet ambient conditions, as shown in Fig. S8.

Paired-pulse facilitation (PPF), excitatory postsynaptic current (EPSC) self-relaxation, and short-term- and long-term-potential (STP and LTP)

In neuroscience, the PPF is an important short-term potentiation phenomenon, which is responsible for the decoding of temporal information in visual or auditory biosignals. The PPF state can be determined as when two excitatory presynaptic spikes are applied to the device in sequence, and so, the second spike, depending on the time interval between the spikes, will create a larger excitatory postsynaptic current (EPSC) than the first spike. In addition, the larger time interval between two spikes will cause a smaller EPSC enhancement, since the PPF effect is induced by the remaining Ca^{2+} concentration triggered by the first spike of presynaptic neuron, which also promotes the total concentration level of Ca^{2+} ions, whereas the second spike of the presynaptic neuron will generate the relative EPSC amplitude upon the time arrival³². The above discussion can be easily followed by the results from guinea pig hippocampal cells studied by Salin et al. and represented in Fig. 5a⁵⁵. In Fig. 5b, we are mimicking the PPF phenomenon in the Pt/n-ZnO/SiO_{2-x}/Pt synaptic heterostructures by similarly applying two identical and non-overlapping spikes. First, we apply one spike (1 ms, -1.25 V) to the device and measure the current response as (A1) amplitude. Later, we send double spikes (same parameters) to the device with the small time interval (~50 μs) between the spikes, and measure the current response as (A2) amplitude. Even though the gain of EPSC, calculated as (A2/A1 ~ 1.11), is quite small, we intentionally apply small spiking parameters (1 ms, -1.25 V) to show that even a low-power spiking operation (~11.25 pW/spike) can be utilized in our synaptic device, which is quite close to that of biological synapses (~10 pW)⁵⁶. This increase in EPSC states could be explained by the drift and accumulation of charged ion species induced by E and Joule heating, as discussed in the section of the resistive switching mechanism. Similar to the biological studies, where the residual effects of Ca^{2+} dynamics, after the first spike arrival, have an impact on the EPSC enhancement when the second spike arrives, indicating further diffusivity and concentration enhancement of the Ca^{2+} ions. For a better illustration of the PPF phenomena, we used separate multiple double spikes (1 ms, -1.5 V) with different time intervals between them. Subsequently, we extract and calculate the EPSC states difference between the first and second spikes and show experimentally the time interval dependence of two applied spikes, as displayed in Fig. 5c. The same analogy of EPSC enhancement can be noted as that of biological systems,

as shown in Fig. 5a. As the time interval between two spikes becomes longer, the accumulated concentration of charged ions species is expected to fully diffuse back to its original equilibrium state; therefore, almost no EPSC improvement is observed. On the other hand, a shorter time interval between two spikes can induce significant EPSC enhancement in the device due to enhanced accumulation of defects. In addition, the time response of PPF characteristics in the device seems to be approximately ten times faster than that in biosynapse, in terms of the interspiking time interval, ranging from μs to ms, whereas in biological systems, it is hundreds of ms. This could potentially be used in neuromorphic architectures operating within high-frequency spiking. In Fig. 5d, we elucidate the synaptic potentiation characteristics, i.e., EPSC enhancement, where identical spikes (1 ms) with varied overall voltage amplitudes (-1.1 V...-1.9 V) were used to observe the gradual synaptic potentiation response of the device. The device EPSC amplitudes were extracted immediately by the small read voltage (0.1 V) after each number of spiking trains applied to the device.

A higher EPSC amplitude is observed when a train of identical spikes is applied to the device with a higher voltage amplitude. This is attributed to the enhanced diffusive dynamics of the charged ion species by high and concentrated E and induced Joule heating effects. Later, when a sufficient number (#200) of identical spikes are applied to the device, the EPSC self-decay characteristics are immediately measured after by the long-time (10 ms) reading voltage (0.1 V) pulse, as shown in Fig. 5e. No matter how high the voltage amplitude with identical spikes applied was, we always observe EPSC self-decay to its initial current level or initial resistance state, connecting it to the “self-back off” diffusion of asymmetric concentration of oxygen vacancies existing in the cone-shaped n-ZnO semiconductor and discussed above. We merely discover that, when a higher voltage of identical spikes are applied to the device, after, the EPSC self-decay is respectively higher and takes a longer time to relax to its original state, which is reasonable since the higher voltage spiking induces a higher concentration and accumulation of charged ion species, which takes a longer time to recombine.

Furthermore, we fit the experimental EPSC self-decay data with the double-exponential function, which is also a part of the stretched-exponential function discussed above in Eq. (5), as follows:

$$I(\Delta t) = I_0 + B_1 \exp\left(-\frac{\Delta t}{\tau_1}\right) + B_2 \exp\left(-\frac{\Delta t}{\tau_2}\right) \quad (6)$$

where I_0 is the constant background, B_1 and B_2 are the prefactors, t_0 is start point time, and τ_1 and τ_2 are the characteristic relaxation times.

Table 2 Summarized parameters of SEF, Eq. (6)

$I_{\text{Self-decay}}/$ parameters	I_0	B_1	B_2	$\tau_1, \text{ ms}$	$\tau_2, \text{ ms}$	t_0
Aft. SET@-1.1V	9.86e-9	9.86e-9	6.62e-9	1.16	33.97	
Aft. SET@-1.5V	7.88e-9	6.64e-9	1.02e-8	1.71	37.35	0.14
Aft. SET@-1.9V	1.20e-8	1.59e-8	1.39e-8	1.87	43.16	

In this case, we can extract the different double-term synaptic memory retention characteristics of the device, as relaxation time τ_1 - being an STP state, and relaxation time τ_2 - being an LTP state, and we summarize the parameters of Eq. (6) in Table 2.

The difference between the τ_1 and τ_2 , time scales is approximately one order of magnitude; therefore, the STP and LTP states could be defined in this time scales differently. Figure 5f shows the transition from STP to LTP by the same frequency but different numbers of identical spikes (-1.9 V , 1 ms) arriving to the device. We observe that after five identical spikes are applied to the device, the EPSC has a rapid drop in the beginning ($\sim 0.1 \text{ ms}$), followed by a fast decrease of the EPSC to its initial state. However, after $N=200$ identical spikes are applied to the device, a higher EPSC change is detected, which also has a rapid drop in the beginning ($\sim 1 \text{ ms}$) but is followed by a long-time ($\sim 100 \text{ ms}$) slow decay of EPSC, indicating that the LTP state can be obtained by HFS spiking with a high number of pulses or by repetitive HFS spiking trains⁵⁷. To further support the LTP state⁵⁸, the device was potentiated by high voltage spiking (-3.75 V , 1 ms , #200), and after, the LTP states were read-out by a small non-disturbing voltage pulse (0.1 V) as shown in Fig. S9. Based on these plasticity behaviors, we further elaborate on the spike-rate- dependent plasticity, namely, the SRDP rule. As displayed in Fig. S10, for the realization of the SRDP rule, we used a fixed number of identical spikes (#7, -1.25 V , 1 ms) with varied time intervals between spikes from 7 ms to $100 \mu\text{s}$. When the time interval between spikes is becoming shorter, the higher transition conductance changes, i.e., a higher EPSC amplitude is observed, indicating the real-time interspiking frequency dependence of the device.

Sliding threshold (θ_m) effect, history-dependent plasticity, and learning experience

We investigate the EPSC amplitude variations depending on the continuous spiking trains arrival from the presynaptic neuron, which are described in two terms, i.e., LFS and HFS, as shown in Fig. S11a. With analog to neuroscience, where the Bienenstock, Cooper, and Munro (BCM) theory⁵⁹ describes the synapse in which synaptic weight (potentiation/depression) exhibits strong

dependence on the frequency of the spiking trains arrival, i.e., APs. Correspondingly, the trigger of gradual transient conduction behavior of the device should be higher at the HFS than at the LFS due to the dynamic short response time of the charged ions, which also closely mimics the Ca^{2+} ions concentration accumulation effects of that in biosynapses. Moreover, high-frequency spiking means small intervals between spikes, during which the charged ion species has no time to decay to their initial state and, as a result, significant accumulation of the charged ion species can be induced in the device. In addition, recent studies based on the resistive switching phenomenon also show a similar frequency dependency in the device's active elements, e.g., WO_x or bilayer $\text{HfO}_y/\text{HfO}_x$ oxides^{60,61}.

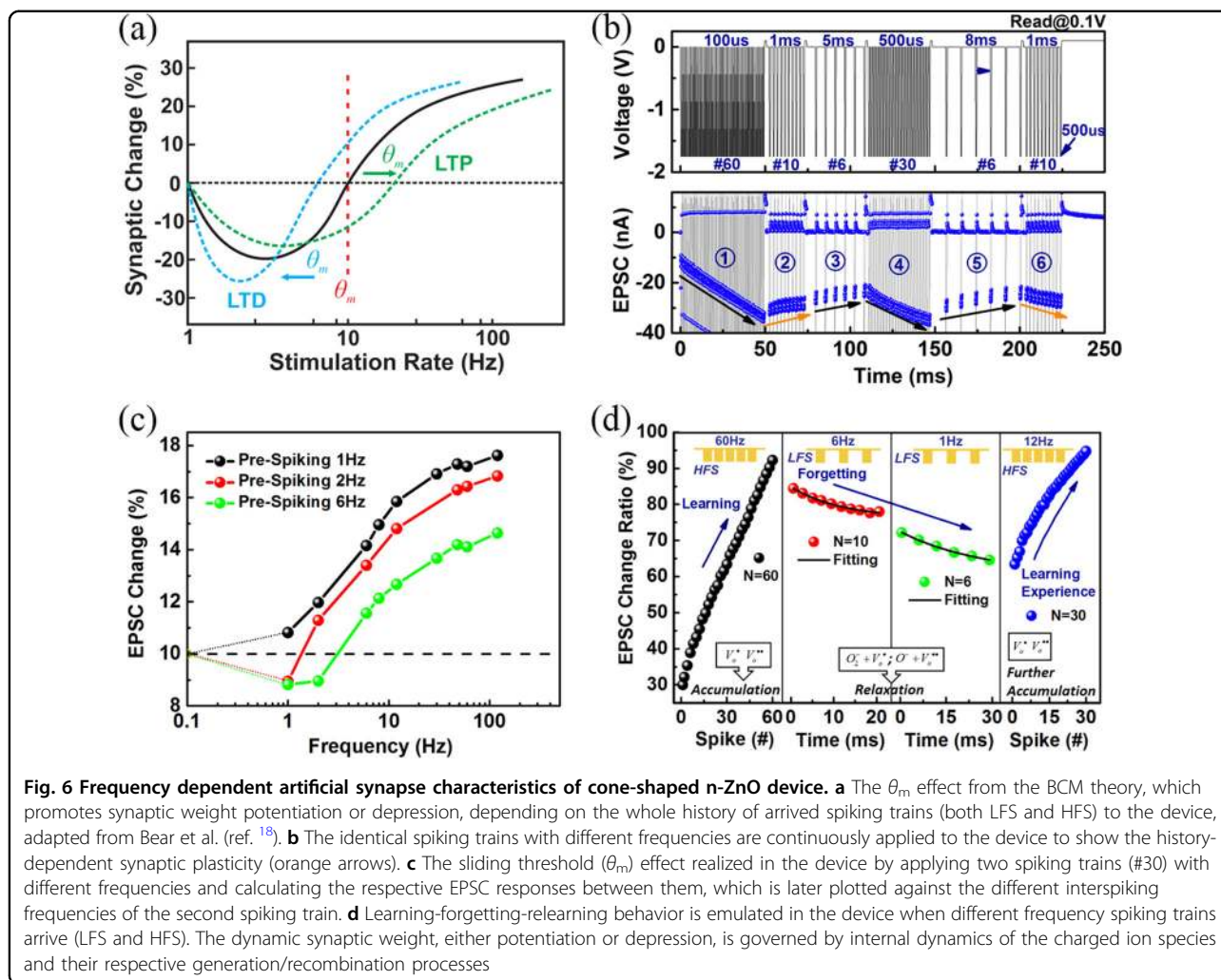
The frequency-dependent synaptic weight change is explored in our Pt/n-ZnO/SiO_{2-x}/Pt synaptic heterostructures, as shown in Fig. S11b. We imply identical spike trains (#50, -1.75 V) with varied interspiking frequencies, and after reading the voltage (0.1 V) of each spiking train, we extract the transient conductance change of the device. Later, we calculate the relative synaptic weight change as follows:

$$\Delta w(\%) = \frac{G_{\text{State}} - G_{\text{Initial}}}{G_{\text{Initial}}} \quad (7)$$

where G_{State} is a conductance state after spiking train arrival, and G_{Initial} is an initial conductance state of the device.

We note that the significant transient conductance change (Δw) of the device can be obtained when the presynaptic neuron firing rate is approximately 30 to 50 Hz, showing that the accumulation of high charged ions with relatively low interspiking frequency can be induced in the device. In addition, the high transient dynamic window ($G_{\text{State}}/G_{\text{Initial}} \sim 4$) can be effectively exploited.

In neuroscience, synaptic plasticity is a dynamic phenomenon, including the overall stimulation history. Particularly, Bear et al.²¹ studied that in biological synapse, HFS typically causes the potentiation of the synaptic weight, whereas LFS typically causes the depression of the synaptic weight. However, importantly, the sliding threshold or modification θ_m , as a function of the spiking trains applied history, exists in the biosynapses of the visual cortex and serves as the stability characteristic of the synaptic dynamic. When a presynaptic neuron constantly sends HFS spiking trains, θ_m shifts to the higher frequency side and increases the threshold for further synaptic potentiation (increase of w_{ij}), i.e., promoting the conditions for synaptic depression (decrease of w_{ij}), whereas, conversely, when the presynaptic neuron constantly sends the LFS spike trains, the θ_m shifts to the lower frequency side and decreases the threshold, i.e., promoting synaptic potentiation rather than synaptic



depression, as shown in Fig. 6a. The important role of the θ_m can be defined as the stability of the synapse, where synaptic plasticity (weight) is governed within a specific dynamic range in contrast to just being saturated at the boundaries. To explore the θ_m effect in our Pt/n-ZnO/SiO_{2-x}/Pt synaptic heterostructures experimentally, we apply groups of identical spiking trains (-1.75 V, 1 ms), while varying the interspike frequencies, and monitor the EPSC change of the device, as shown in Fig. 6b. In step 1, the first spiking train with 60 Hz (to promote HFS) was applied and induced a gradual conductance increase in the device. Next, in step 2, during the spiking train with 6 Hz (to promote LFS), the conductance gradually decreases towards its initial current state of $I_{\text{int}} \sim 0$ A (orange arrow). However, after the spiking activity in 3, 4, and 5 steps, we observe that the same spiking train with 6 Hz can cause the conductance to gradually increase relatively to the initial current state (orange arrow). This implies that not only do the HFS and LFS spiking define the synaptic weight increase/decrease, respectively, but

also the sign and adaptability of the synaptic weight modification, which has an obvious dependence on the history of the applied spikes. To further understand the sliding threshold phenomena, we elaborate an experiment similar to that of Bear et al.'s research²¹. In this experiment we first subject the device to the spiking train (#30) with different interspike frequencies (1, 2, and 6 Hz) separately, and then apply another spiking train (#30) with interspike frequency variations, i.e., from 1 to 120 Hz. Later, we monitor the transient conduction change of the device between the first spiking train (#30) and second spiking train (#30). In the end, we calculate the EPSC change between the first and second spiking trains and plot it against the interspike frequencies of the second spiking train. As shown in Fig. 6c, after the low prespiking frequency (1 Hz), only an increase of the EPSC change is observed in the device, since the next arriving spiking trains all have higher interspike frequencies. On the other hand, when higher frequency prespiking (e.g., 2 and 6 Hz) is applied to the device, both the decrease/increase

of the EPSC change are possible, depending on the interspike frequencies of the recently arriving spiking trains. This results also suggest the evidence of the θ_m effect existing in our device, where the sign of the synaptic weight, either potentiation or depression, is strongly bonded with the history of previously applied spiking trains to the device. Finally, in Fig. 6d, we demonstrate the learning-experience behavior in the device by utilizing identical spiking trains with different frequencies, i.e., HFS and LFS, respectively. First, sixty (#60) negative identical spikes were stimulated to the device and a steep gradual increase of the EPSC was observed, which is considered to be the learning process. Further, by stimulating LFS spiking to the device (6 and 1 Hz), the EPSC decay occurs, where the fitting is consistent with Eq. (5), and which is responsible for the human memory “forgetting curve.” Then, when the next HFS spiking stimulation arrives to the device, a further gradual increase of the EPSC is noted, but now half as much spiking stimuli is required (#30 compare to the first #60) to recover the memory (to induce EPSC increase) to its first learning level; however, the HFS intensity drops from 60 to 12 Hz. Now, the θ_m defines whether HFS or LFS spiking trains arrive to the device, depending on the previous spiking frequency activity. We believe that these types of synaptic behaviors strongly bear the resemblance of the learning process established in biological systems and could probably be adapted in the modern hardware-based neuromorphic systems.

Conclusion

The biorealistic rate-dependent synaptic plasticity, which closely mimics the memory/learning plasticity in biological systems, has been demonstrated in the rectifying diode-like Pt/n-ZnO/SiO_{2-x}/Pt synaptic heterostructures. The important synaptic plasticity behaviors, such as STP and LTP memory retention characteristics, PPF phenomenon, SRDP rule, and θ_m effect, simultaneously exist in the device. The STP and LTP retention were found to be well-fitted with exponential and double-exponential decay functions, resembling “human memory” learning and forgetting characteristics within well-defined time scales. The PPF phenomenon along with the SRDP learning rule were discovered to similarly follow the plasticity behavior of that in biorealistic synapse, thanks to the two critical features of the device, as follows: first, the gradual conductance change in the SET/RESET operations; and, second, the internal ionic dynamics, i.e., diffusion and accumulation of the oxygen vacancies and charged oxygen, which enable analog transient conductance behavior changes via lowering the Schottky diode barrier height. The θ_m effect is explored to show the importance of the biorealistic synaptic weight dynamic stability when numerous spiking trains with either HFS or

LFS are applied to the device; however, the sliding threshold effect dynamically governs the next synaptic weight update according to the history of applied spiking trains. Finally, by utilizing the above synaptic phenomena, we successfully emulate the biorealistic “Learning-Forgetting-Relearning” synaptic behavior. In the future, these findings could help to enable adaptive and dynamic hardware-based neuromorphic systems working in a fashion similar to that of our brain functioning.

Acknowledgements

This research was supported by the Nano Material Technology Development Program through the National Research Foundation of Korea (NRF) funded by the Ministry of science, ICT & Future Planning (NRF-2016M3A7B4910426) as well as by the Future Semiconductor Device Technology Development Program (10080689) funded by MKE/KEIT. We thank Dr. Gul Hassan for helping with the humidity measurement test.

Conflict of interest

The authors declare that they have no conflict of interest.

Publisher's note

Springer Nature remains neutral with regard to jurisdictional claims in published maps and institutional affiliations.

Supplementary information is available for this paper at <https://doi.org/10.1038/s41427-018-0105-7>.

Received: 9 May 2018 Revised: 20 October 2018 Accepted: 26 November 2018.

Published online: 23 January 2019

References

- Hopfield, J. J. & Tank, D. W. Computing with neural circuits-A model. *Science* **233**, 625–633 (1986).
- Adamatzky, A. & Chua, L. *Memristor Networks*. (Springer Science & Business Media, Switzerland, 2013).
- Chua, L. Memristor-the missing circuit element. *IEEE Trans. Circuit Theory* **18**, 507–519 (1971).
- Lee, J. S., Lee, S. & Noh, T. W. Resistive switching phenomena: A review of statistical physics approaches. *Appl. Phys. Rev.* **2**, 031303 (2015).
- Wang, Z. Q. et al. Synaptic learning and memory functions achieved using oxygen ion migration/diffusion in an amorphous InGaZnO memristor. *Adv. Funct. Mater.* **22**, 2759–2765 (2012).
- Torrezan, A. C., Strachan, J. P., Medeiros-Ribeiro, G. & Williams, R. S. Sub-nanosecond switching of a tantalum oxide memristor. *Nanotechnology* **22**, 485203 (2011).
- Yang, J. J., Strukov, D. B. & Stewart, D. R. Memristive devices for computing. *Nat. Nanotechnol.* **8**, 13–24 (2013).
- Abbas, Y. et al. Compliance-free, digital SET and analog RESET synaptic characteristics of sub-tantalum oxide based neuromorphic device. *Sci. Rep.* **8**, 1228 (2018).
- Kim, B. -Y. et al. Nanogenerator-induced synaptic plasticity and metaplasticity of bio-realistic artificial synapses. *NPG Asia Mater.* **9**, e381 (2017).
- Lee, M. J. et al. Synaptic devices based on two-dimensional layered single-crystal chromium thiophosphate (CrPS₄). *NPG Asia Mater.* **1**, pp. 23–30 (2018).
- Kim, S., Choi, S. & Lu, W. Comprehensive physical model of dynamic resistive switching in an oxide memristor. *ACS Nano* **8**, 2369–2376 (2014).
- Jo, S. H. et al. Nanoscale memristor device as synapse in neuromorphic systems. *Nano Lett.* **10**, 1297–1301 (2010).
- Kuzum, D., Yu, S. & Wong, H. P. Synaptic electronics: materials, devices and applications. *Nanotechnology* **24**, 382001 (2013).
- Haykin, S. *Neural Networks and Learning Machines*. (Pearson: Upper Saddle River, NJ, USA, 2009).

15. Yang, J. J. et al. The mechanism of electroforming of metal oxide memristive switches. *Nanotechnology* **20**, 215201 (2009).
16. Burr, G. W. et al. Neuromorphic computing using non-volatile memory. *Adv. Phys.: X* **2**, 89–124 (2017).
17. Wang, Z. et al. Memristors with diffusive dynamics as synaptic emulators for neuromorphic computing. *Nat. Mater.* **16**, 101 (2017).
18. Kim, S. et al. Experimental demonstration of a second-order memristor and its ability to biorealistically implement synaptic plasticity. *Nano Lett.* **15**, 2203–2211 (2015).
19. Kandel, E. R. et al. *Principles of Neural Science. Vol. 4.* (McGraw-hill, New York, NY, 2000).
20. Abbott, L. & Regehr, W. G. Synaptic computation. *Nature* **431**, 796–803 (2004).
21. Bear, M. F. Mechanism for a sliding synaptic modification threshold. *Neuron* **15**, 1–4 (1995).
22. Kirkwood, A., Rioult, M. G. & Bear, M. F. Experience-dependent modification of synaptic plasticity in visual cortex. *Nature* **381**, 526 (1996).
23. Sawa, A. Resistive switching in transition metal oxides. *Mater. Today* **11**, 28–36 (2008).
24. Meyer, R. et al. in *Non-Volatile Memory Technology Symposium, 2008. NVMTS 2008. 9th Annual.* 1–5 (IEEE, Conference Location: Pacific Grove, CA, USA 2008).
25. Aoki, Y. et al. Bulk mixed ion electron conduction in amorphous gallium oxide causes memristive behaviour. *Nat. Commun.* **5**, 3473 (2014).
26. Wang, L. et al. Rectification-regulated memristive characteristics in electron-type CuPc-based element for electrical synapse. *Adv. Electron. Mater.* **3**, pp. 1700063(1–8) (2017).
27. Moon, K. et al. Analog synapse device with 5-b MLC and improved data retention for neuromorphic system. *IEEE Electron Device Lett.* **37**, 1067–1070 (2016).
28. Fujii, T. et al. Electrical properties and colossal electroresistance of hetero-epitaxial SrRuO₃/SrTi_{1-x}Nb_xO₃ (0.0002 ≤ x ≤ 0.02) Schottky junctions. *Phys. Rev. B* **75**, 165101 (2007).
29. Hansen, M. et al. A double barrier memristive device. *Sci. Rep.* **5**, pp. 13753 (1–12) (2015).
30. Graupner, M. & Brunel, N. Calcium-based plasticity model explains sensitivity of synaptic changes to spike pattern, rate, and dendritic location. *Proc. Natl. Acad. Sci.* **109**, 3991–3996 (2012).
31. Shouval, H. Z., Bear, M. F. & Cooper, L. N. A unified model of NMDA receptor-dependent bidirectional synaptic plasticity. *Proc. Natl. Acad. Sci.* **99**, 10831–10836 (2002).
32. Zucker, R. S. & Regehr, W. G. Short-term synaptic plasticity. *Annu. Rev. Physiol.* **64**, 355–405 (2002).
33. Clapham, D. E. Calcium signaling. *Cell* **131**, 1047–1058 (2007).
34. Dahiya, A. et al. Single-crystalline ZnO sheet source-gated transistors. *Sci. Rep.* **6**, 19232 (2016).
35. Huang, Y.-T. et al. In situ TEM and energy dispersion spectrometer analysis of chemical composition change in ZnO nanowire resistive memories. *Anal. Chem.* **85**, 3955–3960 (2013).
36. Janotti, A. & Van de Walle, C. G. Fundamentals of zinc oxide as a semiconductor. *Rep. Prog. Phys.* **72**, 126501 (2009).
37. Rajendran, B. et al. Specifications of nanoscale devices and circuits for neuromorphic computational systems. *IEEE Trans. Electron Devices* **60**, 246–253 (2013).
38. Sheri, A. M., Hwang, H., Jeon, M. & Lee, B. -g Neuromorphic character recognition system with two PCMO memristors as a synapse. *IEEE Trans. Ind. Electron.* **61**, 2933–2941 (2014).
39. Merkle, R. & Maier, J. How is oxygen incorporated into oxides. *Angew. Chem. Int. Ed.* **47**, 2–23 (2008).
40. Qi, J. et al. Resistive switching in single epitaxial ZnO nanoislands. *ACS Nano* **6**, 1051–1058 (2012).
41. Carrasco, J., Lopez, N. & Illas, F. First principles analysis of the stability and diffusion of oxygen vacancies in metal oxides. *Phys. Rev. Lett.* **93**, 225502 (2004).
42. Janotti, A. & Van de Walle, C. G. Oxygen vacancies in ZnO. *Appl. Phys. Lett.* **87**, 122102 (2005).
43. Chen, J. -Y. et al. Dynamic evolution of conducting nanofilament in resistive switching memories. *Nano Lett.* **13**, 3671–3677 (2013).
44. Huang, C. -H. et al. Manipulated transformation of filamentary and homogeneous resistive switching on ZnO thin film memristor with controllable multistate. *ACS Appl. Mater. Interfaces* **5**, 6017–6023 (2013).
45. Allen, M. & Durbin, S. Influence of oxygen vacancies on Schottky contacts to ZnO. *Appl. Phys. Lett.* **92**, 122110 (2008).
46. Cowan, W. M., Südhof, T. C. & Stevens, C. F. *Synapses* (JHU Press, Baltimore, Maryland 2001).
47. Burgoyne, R. D. Neuronal calcium sensor proteins: generating diversity in neuronal Ca²⁺ signalling. *Nat. Rev. Neurosci.* **8**, 182 (2007).
48. Wickelgren, W. A. Trace resistance and the decay of long-term memory. *J. Math. Psychol.* **9**, 418–455 (1972).
49. Huang, Y. -J. et al. Dual-functional memory and threshold resistive switching based on the push-pull mechanism of oxygen ions. *Sci. Rep.* **6**, 23945 (2016).
50. Vanheusden, K. et al. Mechanisms behind green photoluminescence in ZnO phosphor powders. *J. Appl. Phys.* **79**, 7983–7990 (1996).
51. Sze, S. M. & Ng, K. K. *Physics of Semiconductor Devices.* (John Wiley & Sons, Inc., Hoboken, New Jersey 2007).
52. Rubin, D. C. & Wenzel, A. E. One hundred years of forgetting: A quantitative description of retention. *Psychol. Rev.* **103**, 734 (1996).
53. Wixted, J. T. & Ebbesen, E. B. On the form of forgetting. *Psychol. Sci.* **2**, 409–415 (1991).
54. Lamprecht, R. & LeDoux, J. Structural plasticity and memory. *Nat. Rev. Neurosci.* **5**, 45–54 (2004).
55. Salin, P. A., Scanziani, M., Malenka, R. C. & Nicoll, R. A. Distinct short-term plasticity at two excitatory synapses in the hippocampus. *Proc. Natl. Acad. Sci.* **93**, 13304–13309 (1996).
56. Bliss, T. V. & Collingridge, G. L. A synaptic model of memory: long-term potentiation in the hippocampus. *Nature* **361**, 31 (1993).
57. Chang, T., Jo, S. -H. & Lu, W. Short-term memory to long-term memory transition in a nanoscale memristor. *ACS Nano* **5**, 7669–7676 (2011).
58. Abraham, W. C. How long will long-term potentiation last? *Philos. Trans. R. Soc. Lond. B: Biol. Sci.* **358**, 735–744 (2003).
59. Bienenstock, E. L., Cooper, L. N. & Munro, P. W. Theory for the development of neuron selectivity: orientation specificity and binocular interaction in visual cortex. *J. Neurosci.* **2**, 32–48 (1982).
60. Du, C., Ma, W., Chang, T., Sheridan, P. & Lu, W. D. Biorealistic implementation of synaptic functions with oxide memristors through internal ionic dynamics. *Adv. Funct. Mater.* **25**, 4290–4299 (2015).
61. Yin, J. et al. Adaptive crystallite kinetics in homogenous bilayer oxide memristor for emulating diverse synaptic plasticity. *Adv. Funct. Mater.* **28**, 1706927 (2018).